ACS APPLIED NANO MATERIALS

www.acsanm.org

Article

Fluorescent Boron Oxide Nanodisks as Biocompatible Multi-messenger Sensors for Ultrasensitive Ni^{2+} Detection

Angela Terracina, Nicolò Mauro, Juliette Le Balle, Radian Popescu, Michelangelo Scopelliti, Gianpiero Buscarino, Mara A. Utzeri, Marco Cannas, Gennara Cavallaro, Fabrizio Messina, and Alice Sciortino*

Cite This: *ACS Appl. Nano Mater.* 2023, 6, 6036–6045

Read Online

ACCESS | Metrics & More | Article Recommendations | Supporting Information

ABSTRACT: Boron-based nanocomposites are very promising for a wide range of technological applications, spanning from microelectronics to nanomedicine. A large variety of B-based nanomaterials has been already observed, such as borospherene, B nanotubes and nanoparticles, and boron nitride nanoparticles. However, their fabrication usually involves toxic precursors or leads to very low yields or small boron atom concentration. In this work, we report the synthesis of nanometric B_2O_3 nanodisks, a family of nanomaterials with a quasi-2D morphology capable of intense fluorescence in the visible range. Such as boron-based nanomaterial, which we synthesized by pulsed laser ablation of a boron target, is water-dispersible and nontoxic, and displays a highly crystalline structure. Moreover, its bright blue photoluminescence is highly sensitive and selective for the presence of Ni^{2+} ions in solution, down to extremely small concentrations in the picomolar range. The results are very promising in view of the use of such novel B_2O_3 nanodisks as ultrasensitive multi-messenger Ni^{2+} nanosensors.

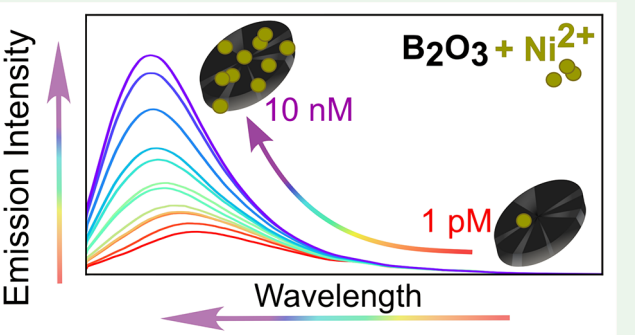

KEYWORDS: *boron oxide, boron nanocomposites, nanosensors, nickel detection, multi-messenger sensor*

1. INTRODUCTION

Boron is a light chemical element able to form covalent-bonded molecular networks with a wide variety of structures.[1] Bulk boron has been industrially employed in many different areas, such as high-density fuels,[2,3] protective coatings,[4] semiconductors,[5,6] microelectronics,[7] and refractory materials.[8,9] Furthermore, both elemental boron and its compounds have found interesting biomedical applications, especially in neutron capture therapy for cancer treatment in the currently under development field of nanomedicine.[10−12] When going down to the nanometric scale, boron-based nanomaterials appear in a wide variety of forms: nanoribbons,[13] nanotubes,[14,15] nanowires, and nanofibers,[16−18] and the recently discovered borospherene[19,20] and borophene[21,22] that are B-based analogues of fullerene and graphene, respectively, as well as quasi-spherical nanoparticles (NPs), both crystalline and amorphous.[23−25] Additionally, several B-containing nanocompounds have attracted great interest from researchers, such as the well-known hexagonal boron nitride (h-BN),[26] rare-earth borides,[27] Kondo topological insulators,[27,28] or recently synthesized boron oxide nanoparticles, which have been proposed as additives to enhance electrochemical,[29] mechanical, and thermal properties in certain composite materials.[30] Despite the large interest in exploring and understanding all of these B-based nanostructures, experimental investigations in boron nanoscience are still relatively limited as compared to theoretical studies (with the exception of h-BN).[1] In particular, only a handful of works have reported the synthesis of B_2O_3 nanoparticles so far because of a surprising lack of available synthetic methods.[31]

In regard to synthesis routes, several different techniques and precursors have been used to obtain boron-based nanoobjects, often involving the use of highly toxic gases or compounds,[24] such as arc decomposition of diborane,[32] gas phase reduction of boron trichloride,[33] solution reduction of boron tribromide,[24] gas phase pyrolysis of decaborane,[34] and many others.[35] Another issue is that large quantities of the final boron compounds are often needed for medical applications, raising the issue of the possible toxicity problems raised by such nanomaterials in living organism. Thus, one of the open

Received: January 26, 2023
Accepted: March 27, 2023
Published: April 3, 2023

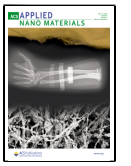

Downloaded via 37.116.232.13 on April 28, 2023 at 08:41:03 (UTC).
See https://pubs.acs.org/sharingguidelines for options on how to legitimately share published articles.

© 2023 The Authors. Published by American Chemical Society

https://doi.org/10.1021/acsanm.3c00383
ACS Appl. Nano Mater. 2023, 6, 6036−6045

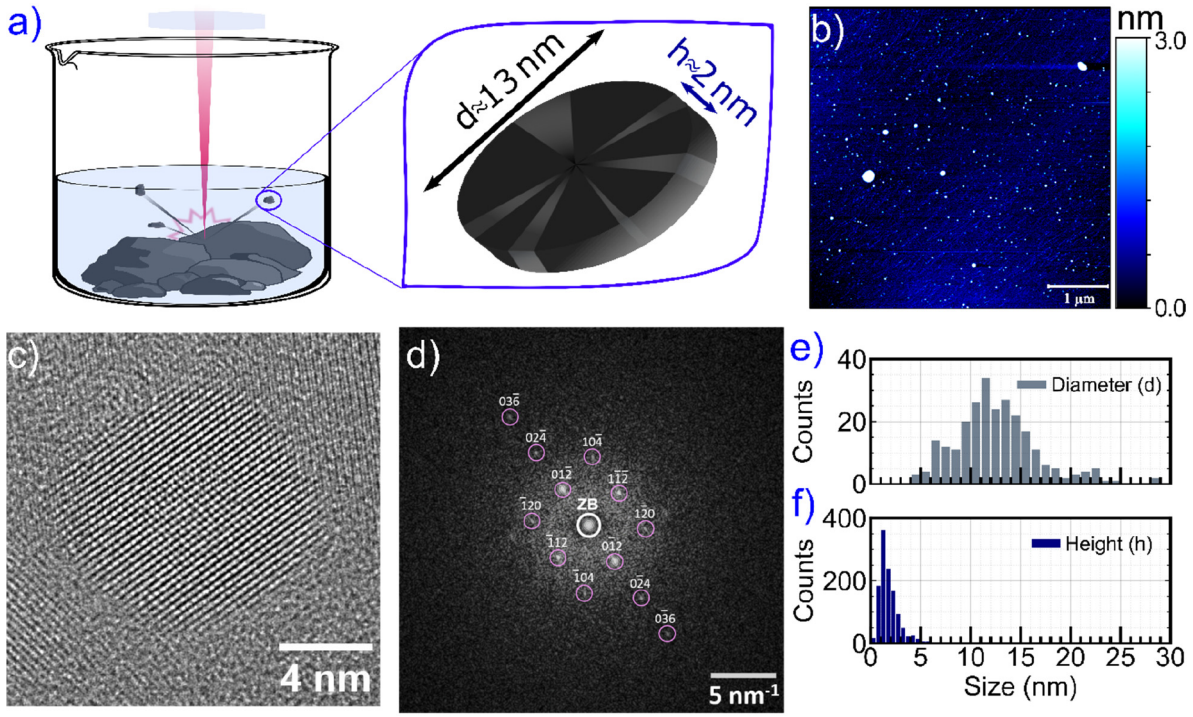

Figure 1. Morphological characterization of BONDs. (a) Illustrative scheme of the laser ablation carried out on millimetric crystalline boron chunks in water, leading to the formation of the BONDs. (b) AFM image of BONDs on a mica substrate. (c) HRTEM image of an individual monocrystalline BOND and (d) its corresponding FT with calculated diffraction pattern with Miller indices for bulk hexagonal B_2O_3 in the [421]-zone axis. Histograms of (e) the diameter distribution estimated from HRTEM images and (f) the height distribution derived from AFM images.

challenges in this field is devising green synthesis pathways of B-based NPs which can avoid as much as possible the contamination of the final target by toxic side products or unreacted precursors without compromising the control of the particles size or their crystallinity.[1,36,37] In this context, pulsed laser ablation in liquid (PLAL) is gaining interest as an emerging technique for nanomaterial synthesis. In fact, PLAL is known as a green method to synthesize nanomaterials.[38] Among the many advantages of PLAL, there are its versatility, low cost, and ease of execution.[38] In addition, PLAL allows control to a certain extent of the amount of oxidation of the final nanomaterials,[39] guarantees a high batch-to-batch reproducibility,[38] and allows production of stable particles in solution without the addition of ligand protection,[40] avoiding contamination issues of their surfaces.[36,41] The synthesis rate depends on laser pulse characteristics as repetition rate, the energy/pulse, and the specific used wavelength.[38]

Here we use PLAL of a boron target in water as a green route to achieve, for the first time, the synthesis of a novel type of B-based nanomaterial, consisting of photoluminescent B_2O_3 nanodisks. A thorough characterization of these nanomaterials by an arsenal of different experimental techniques reveals a range of interesting properties. B_2O_3 nanodisks display a highly crystalline structure, emit luminescence peaking at 440 nm, are stable in aqueous suspension, and are biocompatible in a proof-of-principle in vitro study. The biocompatibility is quite interesting considering that boron oxide is considered an irritant for eyes and for the respiratory system according to National Institute for Occupational Safety and Health (NIOSH). In addition, they display exceptional sensitivity to Ni^{2+} in solution, which is highly appealing for (bio)sensing technologies. Similarly to other heavy metals, Ni^{2+} is one of the most severe environmental contaminants of the environment, food, and living organisms[42,43] because of accumulation phenomena like biomagnification.[44] Here we find that B_2O_3 nanodisks selectively respond to tiny (1 pM) concentrations of Ni^{2+} through correlated variations of the fluorescence peak position, intensity, and excited-state lifetime, which make such nanoparticles multi-messenger nanosensors of Ni^{2+} ions, with competitive performance as compared to state-of-the-art detection methods. The results are very promising in view of the engineering of boron-based nanomaterials for nanosensing and other prospective nanotechnologies. In fact, the important ease of the synthesis of our nanosensors constitutes a noteworthy matter of interest in the field of environmental monitoring, since it typically requires a huge implementation scale to be really useful.[45]

2. EXPERIMENTAL METHODS

2.1. Materials and Sample Synthesis. Materials: millimetric boron crystals, nickel(II) sulfate, cobalt(II) nitrate, copper(II) sulfate, silver nitrate, zinc(II) sulfate, and Fe(III) sulfate have been purchased from Sigma-Aldrich. Human bronchial epithelial cell line (16-HBE) was purchased from Sigma-Aldrich (Milan, Italy) and cultured in supplemented Dulbecco's Minimum Essential Medium (DMEM) (EuroClone, Milan, Italy) supplemented with 10% fetal bovine serum (FBS, EuroClone, Milan, Italy), 1% penicillin/streptomycin (10 000 U mL^{-1} and 10 mg mL^{-1} respectively, EuroClone, Milan, Italy), and 1% L-glutamine (EuroClone, Milan, Italy), at 37 °C in a 5% CO_2 humidified atmosphere. Cell Titer 96 Aqueous One Solution Cell Proliferation assay (MTS solution) was purchased from Promega (Madison, WI, USA).

Synthesis of B_2O_3 nanodisks: We performed pulsed laser ablation in liquid (PLAL) by using a Q-switched Nd:YAG pulsed laser (Quanta System SYL-201) with a 10 Hz pulse frequency, a 5 ns pulse width, a pulse peak at 1064 nm, and about a 100 mJ pulse energy (see Figure 1a). The laser beam has been focused by using a spherical lens so that the focus position matches as much as possible the surface of

https://doi.org/10.1021/acsanm.3c00383
ACS Appl. Nano Mater. 2023, 6, 6036−6045

the boron crystals that are covered by ultrapure water. The target sample was placed on a slow-spinning plate (0.1 Hz) in order to scan the ablating laser beam over the entire surface of the boron target. The ablation was carried out for about 48 h. At the end of the process, the suspension was separated from macroscopic boron by centrifugation at 10 000 rpm and the supernatant was finally filtrated by using syringe filters of 200 nm and then of 20 nm. The synthesis rate is 3−4 mg/h.

2.2. Structural and Morphological Characterization. High-resolution transmission electron microscopy (HRTEM): The crystal structure of the sample was investigated by high-resolution (HR) transmission electron microscopy (TEM) performed on an FEI Titan^3 80−300 aberration-corrected microscope at a 300 keV electron energy. HRTEM images were evaluated by calculating the two-dimensional Fourier transform (FT), which yields information on the crystal structure of single nanoparticles. The analysis was performed by comparing the experimental FT and the calculated diffraction patterns with Miller indices, where the latter was obtained by using the Jems (Java version of the electron microscopy simulation) software.[46] The zero-order beam (ZB) is indicated by using a white circle.

X-ray photoelectron spectroscopy (XPS) analysis was performed on freshly prepared ablated boron, deposited by drop-casting on aluminum plates, by means of a PHI 5000 VersaProbe II (ULVAC-PHI, Inc.), using an Al anode (Al K_α 1486.6 eV), a 100 μm diameter beam (15 kV, 25 W) and keeping the sample at 45° with respect to the analyzer (128 channels hemispherical analyzer, operating in FAT mode). During the data analysis, the charge was compensated by both electron and argon ion beams. The used pass energy (PE) was 117.400 eV for survey scans (energy resolution: 1.000 eV), while for high resolution spectra (resolution: 0.050 eV) PE was kept at 23.500 eV. The energy scale was corrected using as a reference the C−C/C−H peak of the adventitious carbon (284.80 eV). Data were analyzed using Multipak 9.9.2 (ULVAC-PHI, Inc.) using a Shirley background and a Gauss-Lorentz line shape for the observed species.

Attenuated total reflection (ATR) spectra were measured by using a Bruker Platinum ATR spectrometer equipped with a single reflection diamond crystal in the range 4,000−400 cm^{-1}. A single drop of sample solution was deposited onto the sample holder and let dry before the measurement. We recorded a background measurement with 24 scans in order to subtract it to the sample measurement (same parameters).

Fourier transform infrared (FTIR) spectroscopy measurements were carried out with a FT/IR 7600−JASCO spectrometer (JASCO Corporation, Tokyo, Japan) under an inert nitrogen atmosphere, depositing sample droplets on a silica support.

Atomic force microscopy (AFM) measurements were acquired on a sample obtained by depositing a drop of an aqueous solution of B_2O_3 particles on a mica substrate. AFM measurements were performed at room temperature with a Bruker Dimension FastScan Microscope working in soft tapping mode by using FastScan A probes (Bruker) with a tip radius approximately equal to 5 nm. AFM images were obtained with a tip velocity of 15 μm/s and a target amplitude of about 15 nm. The pixel resolution was fixed at about 1024 × 1024 points.

Differential scanning calorimetry (DSC) coupled with thermogravimetric analysis (TGA) was performed using a DSC/TGA 131 EVO (by SETARAM Instruments). Measurements were carried out on BOND sample using about 6 mg of sample in a closed alumina crucible under nitrogen atmosphere (flow rate 1 mL min^{-1}). The heating rate applied was 10 °C min^{-1} in the range 30−560 °C. Thermograms were normalized to the unit weight.

Zeta potential evaluation by dynamic light scattering (DLS) analysis was achieved by aqueous electrophoresis measurements using a Malvern Zetasizer NanoZS instrument equipped with a 632 nm laser with a fixed scattering angle at 173 °C. The analysis was performed on BOND dispersion in 0.01 mM KCl at 25 °C. The zeta-potential values (mV) were calculated from electrophoretic mobility using the Smoluchowski relationship.

2.3. Optical Analysis. Steady-state optical absorption (OA) spectra of BOND solutions were acquired in 1 cm quartz cuvette by an optical fiber spectrometer (Avantes AvaSpec-uls2048cl-evo-rs) in the range 200−1300 nm.

Time-resolved photoluminescence (TRPL) of BONDs was investigated using the following setup: a monochromator (Spectra Pro2300i PI Acton), a time-gated CCD camera (PI-MAX), and a tunable pulsed laser (Opotex Vibrant) with a 10 Hz pulse frequency and a 5 ns pulse width. Laser and CCD spectroscopy were synchronized in order to acquire steady-state photoluminescence (PL) spectra as a function of time delay after photoexcitation. The emission intensity is recorded at a variable delay after the photoexcitation during a 1 ns temporal window. PL lifetimes were extracted by least-squares fitting of the temporal kinetics of the PL intensity. In order to obtain steady state emission spectra, we recorded the spectrum with a temporal window of 100 ns, exciting at 350 nm. The accuracy of the lifetime is 0.2 ns.

The emission efficiency of BONDs was evaluated by the estimation of their quantum yield (QY), while fluxing N_2, in comparison with Coumarin 2 (purchased by Lambda Physik) diluted in water, having a similar emission range and a QY = (94 ± 9)%.

2.4. Biological Studies. In vitro cytocompatibility assay: the cytocompatibility of BONDs was evaluated by MTS assay on a human bronchial epithelial cell line (16-HBE). Cells were incubated in a 96 wells plate at a density of 1.5 × 10^4 cells/well (200 μL) and grown in supplemented Dulbecco's Minimum Essential Medium (DMEM) for 24 h at 37 °C and 5% CO_2. Then, the medium was replaced with a dispersion of BONDs in DMEM (200 μL) in the concentration range 1000−25 μg mL^{-1}. After 24 and 48 h of incubation, the dispersion was removed and each well was washed three times with Dulbecco's phosphate-buffered saline (DPBS) at pH 7.4. Then, cell viability was evaluated by MTS assay, adding to each well 120 μL of MTS assay solution (DMEM/MTS 6:1). Then, cells were incubated for an additional 2 h at 37 °C and 5% CO2 before reading the absorbance at 492 nm using a Microplate Reader (Multiskan Ex, Thermo Labsystems, Finland). Cell viability was expressed as percentage of living cells compared to the untreated control of seeded cells (100% of cell viability). All biological experiments were performed in triplicate.

3. RESULTS AND DISCUSSION

Figure 1a depicts the synthesis and the morphological characterization of the boron-based nanoparticles prepared by pulsed laser ablation in the liquid phase (PLAL). The PLAL of a Boron target in water via high intensity nanosecond near-infrared laser pulses generates a dark solution that contains the B-based nanoparticles (see Experimental Section for more details). This sample was first processed through 200 and 20 nm filters in order to remove the larger aggregates, and then extensively analyzed by different structural and morphological techniques.

Figure 1b shows a representative AFM image acquired from the sample drop-cast on a mica substrate. The image displays several hundred isolated nanoparticles spread over the probed area (25 μm^2). By analyzing the height distribution over a population of about 1200 nanoparticles, we determine an average height h of about 1.9 nm (Figure 1f). Moreover, we performed high resolution AFM measurements on a smaller area (1 μm^2) where we found fewer particles than expected and they looked like flat disks as shown in Figure S1. To further investigate the structure of these nanoobjects, we performed HRTEM measurements. Figure 1c, d shows the HRTEM image of a single nanoparticle and its corresponding Fourier Transform (FT). The high degree of crystallinity of this nanoparticle is evident in the HRTEM image (Figure 1c). In fact, the whole particle represents a single monocrystal with a B_2O_3 hexagonal structure (Figure S3) as indicated by the

https://doi.org/10.1021/acsanm.3c00383
ACS Appl. Nano Mater. 2023, 6, 6036−6045

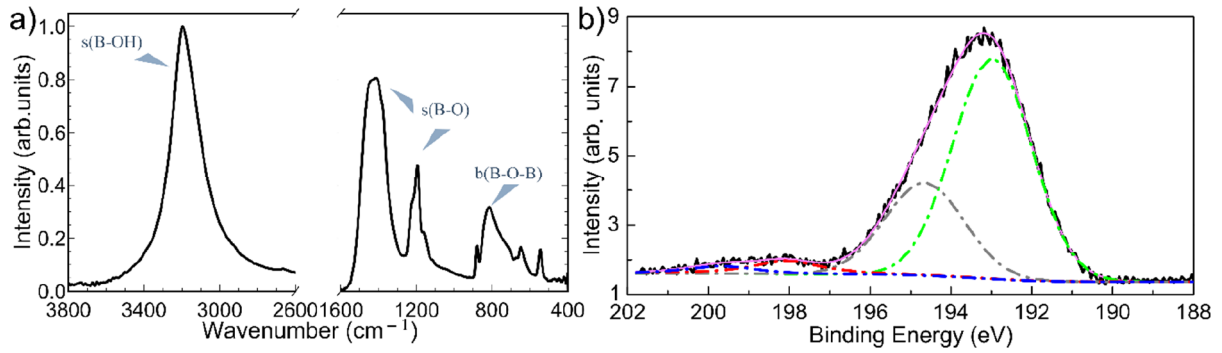

Figure 2. (a) ATR spectrum acquired for the BONDs. (b) XPS spectrum of B 1s region acquired for the BONDs (black line) and compared to the simulated spectrum (pink line) obtained by summing four Gaussian contributions (dashed lines) peaked at 199.5, 198.0, 195.0, and 193.0 eV respectively. The distributions peaked at 193.0 and 195.0 eV concern the B 1s region, and those peaked at 198.0 and 199.5 eV concern the Cl 2p region.

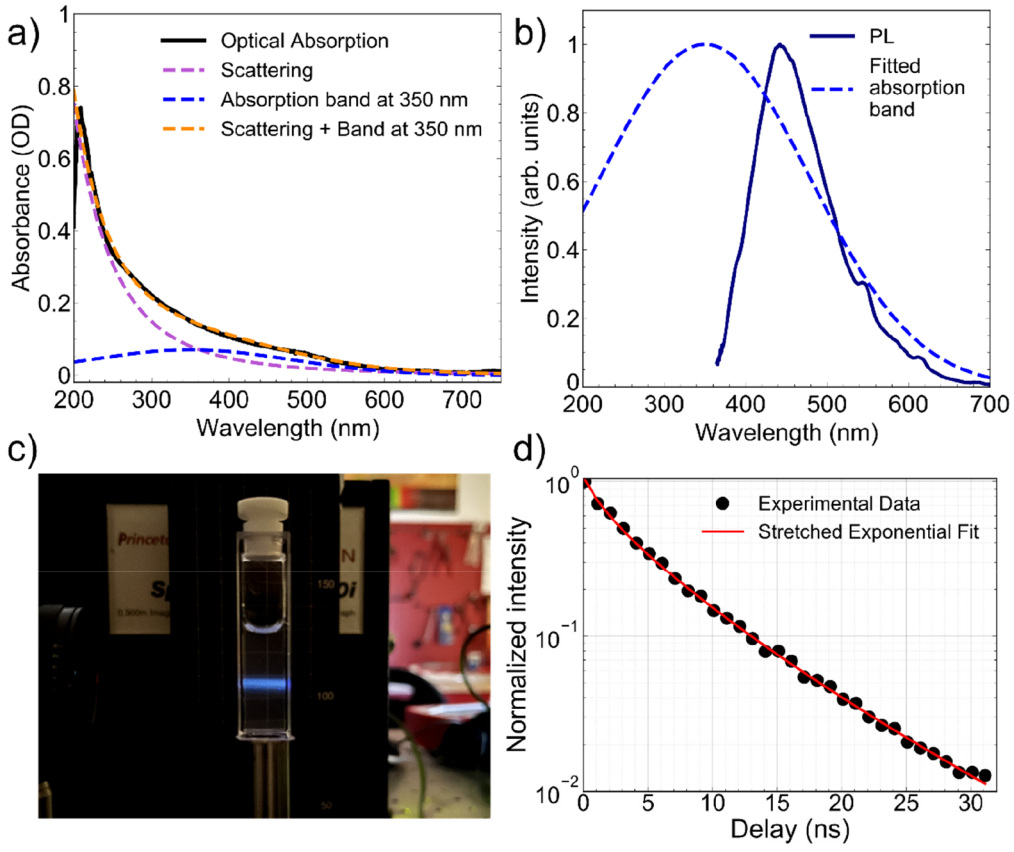

Figure 3. Optical characterization of BONDs. (a) Absorption spectrum (black line) and different simulated contributions: Rayleigh scattering (violet), absorption band (blue), and the sum of both (orange). (b) Photoluminescence spectrum (full line) compared with the simulated Gaussian absorption band (dashed line). (c) Photographic picture of a colloidal suspension of BONDs in water when irradiated by a 350 nm laser beam. (d) Excited-state decay dynamics obtained experimentally (black dots) superimposed on the best fitting curve (red line).

good agreement between its 2-dimensional FT and the calculated diffraction pattern of bulk hexagonal B_2O_3 (space group *P*3121, space group number 152, lattice parameters of a = 4.3351 Å and c = 8.3414 Å[47]) in the [421]-zone axis (Figure 1d). An overview HRTEM image acquired on a large area of the sample (Figure S2) confirms the presence of many crystalline B_2O_3 nanoparticles with different orientations. Accordingly, the FT pattern (Figure S2) calculated from this image shows Debye−Scherrer rings, which perfectly match the expected pattern of bulk hexagonal B_2O_3.[47] This demonstrates the formation of NPs with the same B_2O_3 crystalline structure and, by extension, the structural homogeneity of the produced nanomaterial. Moreover, the histogram of the diameter distribution obtained by the evaluation of about 250 NPs recorded on several HRTEM images with different magnifications is shown in Figure 1e. From these data (Figure 1e), we calculated an average particle diameter, d, of about 13 nm.

Taking into account that the average height h of these B_2O_3 NPs of h < 2 nm is almost 1 order of magnitude smaller than their average diameter d = 13 nm their morphology is better pictured as boron oxide nano-disks (BONDs) rather than standard spherical particles. The synthesis of so small boron

https://doi.org/10.1021/acsanm.3c00383
ACS Appl. Nano Mater. 2023, 6, 6036−6045

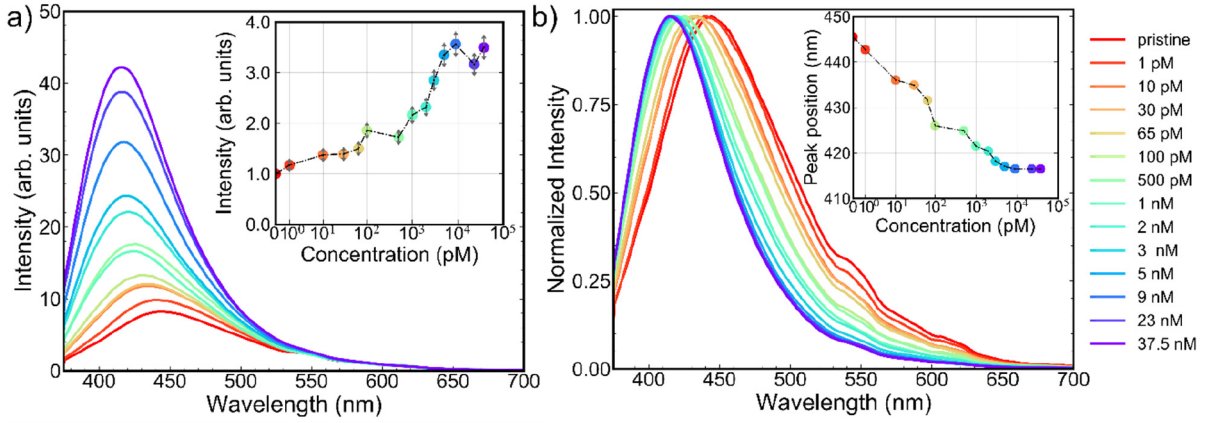

Figure 4. (a) PL spectra acquired for BONDs on increasing Ni^{2+} concentration (from red to violet). In the inset, the peak intensity is plotted as a function of the concentration. (b) The same spectra of panel a normalized by each peak intensity. In the inset, the position of the peak is shown as a function of Ni^{2+} concentration.

oxide nano-objects is in itself very unusual in the literature,[1,31] and in addition, previous reports have never observed nano-B_2O_3 with the quasi-flat morphology found here. Indeed, to the best of our knowledge, this is the first report on the synthesis of monocrystalline B_2O_3 nanodisks.

To further investigate the chemical structure of BONDs, we performed ATR and XPS measurements. Figure 2a shows a typical ATR spectrum acquired from the BONDs. The spectrum contains different peaks that can be attributed to B−OH stretching (3200 cm^{-1}), most likely due to the B−OH groups terminating the surface of the NPs. We also observe several B−O−B bending (730−870 cm^{-1}) and B−O stretching (1160−1220 cm^{-1} and 1380−1450 cm^{-1}) vibrational modes of the bulk B_2O_3 structure.[48]

Concerning XPS, we acquired high resolution spectra of the B 1s region and survey (1100.0−0.0 eV), displayed in Figure 2b and Figure S4, respectively. XPS survey scans reveal an atomic composition of O 53.61 atom %, B 23.21 atom %, and C 21.07 atom %, and traces of Na, N, S, and Cl impurities.

The energy scale of the spectra was corrected using as an internal reference the adventitious carbon C−C/C−H peak (C 1s region, 284.80 eV, not shown). The B 1s region analysis shows an overlap of different groups of signals: a main peak, around 193 eV, assigned to boron; and a much smaller peak, around 198 eV, identified as a Cl impurity. The observed B signal consists mainly of two species: the first one (192.98 eV; ca. 70% of the B atoms) was identified as B_2O_3, while the second one (194.65 eV) shows an unusually high BE value, indicating a strong electron withdrawal from B species. This would indicate that the boron is bound to a relatively high number of oxygen atoms, suggesting a perborate-like environment. Consistently, the stoichiometric ratio between boron and oxygen found from the survey scans (B:O ≈ 0.43) is lower than that expected for the B_2O_3 structure (B:O = 0.66), pointing to an excess of oxygen. Such excess of oxygen could also be due to boron vacancies within the bulk of the crystalline structure and to the plentiful −OH groups present on the surface, as revealed by ATR. It is also possible to observe a shakeup peak ($\pi \rightarrow \pi^*$) around 198 eV, indicating the presence of an extended network.

DSC/TGA experiments (Figure S5 and Table S1) show that the sample is stable until 95 °C. It loses 58% of the mass in correspondence of two endothermic peaks at 150 and 173 °C. Such a relatively low threshold temperature for weight loss suggests that nanodisks probably release water molecules eventually adsorbed on the surface, together with hydroxyl functional groups linked with surface boron atoms. After this loss, the sample is thermally stable until at least 600 °C. We verified that the optical properties (vide infra) are not modified by a thermal treatment up to 180 °C (not shown). Thus, the overall picture emerging from AFM, HRTEM, XPS and FTIR-ATR is that the obtained sample is composed of B_2O_3 monocrystalline nanodisks strongly oxidized on the surface. The negative surface structure is confirmed by zeta potential experiments which reveal a ξ-potential of −30 ± 10 mV, guaranteeing a high colloidal stability of BONDs in water.

After the chemical and morphological characterizations were completed, we addressed the optical properties of the BONDs. In Figure 3a the optical absorption spectrum of a diluted aqueous solution of BONDs (8 mg/L) is shown. At a first glance, the spectrum appears very broad and non clearly resolvable, although the presence of an absorption band in the near-UV is hinted at by the inflection of the spectrum in this region. By carrying out an appropriate fit, the absorption spectrum results indeed to be the sum of a Rayleigh scattering contribution ($y = 1/\lambda^4$) plus a weak and broad Gaussian band peaked at 350 nm, as shown in Figure 3a. Photoexciting the sample at 350 nm, a clear blue fluorescence (PL) is observed (Figure 3c). Figure 3b shows the PL spectrum, peaking at λ_{peak} = 445 nm with a bandwidth of about 110 nm. By comparing the emission intensity with that of Coumarin 2 (QY = 94%) recorded under identical conditions, we found that boron oxide nanoparticles have a relatively low QY, equal to about 1% when fluxing nitrogen in solution. We believe it should be possible to increase the efficiency with some surface passivation which should help to protect the surface and to avoid non-radiative losses. However, the rest of the analysis was carried out on the as-grown sample. We also measured the decay kinetics of the emission band, shown in Figure 3d, where the excited-state dynamics has been fitted by a stretched-exponential law $I(t) = I_0\exp(-(t/\tau)^{\beta})$, obtaining a lifetime τ = (4.0 ± 0.2) ns and a significant stretching factor $\beta \approx 0.75$. Such a large stretching is a typical behavior of disordered systems and not uncommon in small emissive nanocrystals,[49] being very different from the single-exponential excited-state decay behavior of archetypal fluorophores in solution phase. This stretched-exponential trend is also consistent with the very broad emission band that we observed (Figure 3b). Despite

https://doi.org/10.1021/acsanm.3c00383
ACS Appl. Nano Mater. 2023, 6, 6036−6045

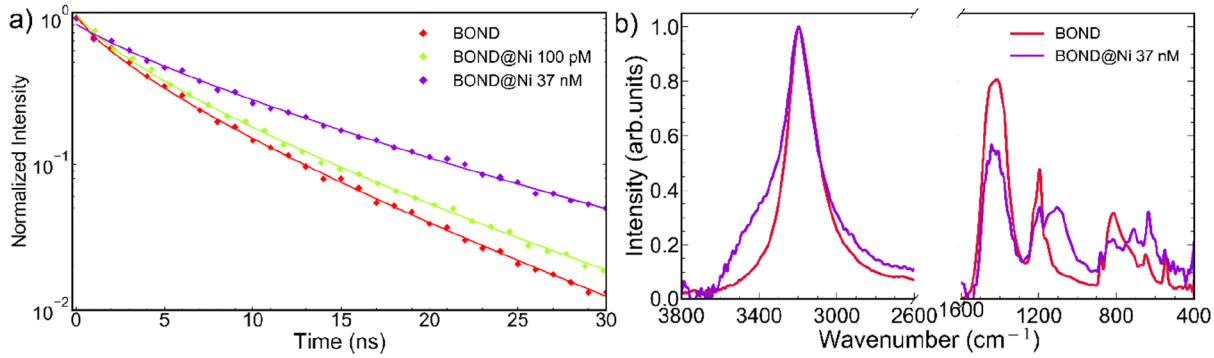

Figure 5. (a) Comparison of excited-state decay dynamics between pristine BONDs and two BOND samples in the presence of different Ni^{2+} concentrations. The dotted lines are the experimental data, whereas the continuous lines are the results of the stretched-exponential fits. (b) Comparison of ATR spectra for pristine BONDs (red line) and BOND@Ni (37 nM, violet line).

this inhomogeneity, the decay is independent of the emission wavelength, and thus the band decays all together, indicating the existence of a single type of chromophore, albeit its heterogeneity. Therefore, the emissive centers responsible for the emission of BONDs either experience a heterogeneous local environments or they have themselves a significant degree of structural heterogeneity. The electronic structure of B_2O_3 is still being debated. The bandgap of its bulk form is found to be at 5.02 eV,[50] or it can be even higher as a function of the specific structure.[51] Here, we found an optical transition that can be excited at 350 nm (3.5 eV) which is below the hypothesized threshold. Thus, it is reasonable to associate the blue emission to an optical transition related to some intragap states due to some structural vacancies as boron vacancies or to some interstitial oxygen defects.

We found that BONDs display an exceptional sensitivity to the detection of tiny amounts of nickel ions in the solution phase. Figure 4 shows the effects on the emission band upon the introduction of very small concentrations of Ni^{2+} ions into the solution containing the BONDs. By monitoring the PL intensity, a gradual increase has been observed (Figure 4a) by adding Ni^{2+} ions, as well as a blue-shift of the peak position (Figure 4b). Clear changes of the optical properties can be seen while the Ni^{2+} concentration is as low as 1 pM, corresponding to about 60 pg/L or a part per quadrillion (ppq) in weight. Such progressive spectroscopic changes are observed until saturation develops when Ni^{2+} concentration amounts to 10 nM. At such concentration, the sample reaches an emission peak position of 417 nm, which is 28 nm blue-shifted compared to the emission peak measured in the pristine sample (before Ni^{2+} addition), and an intensity ~3.5 times larger than that of the bare BONDs.

The substantial changes we observe in the spectroscopic properties indicate a very strong and selective interaction between the BONDs and Ni^{2+} ions. In fact, we carried out similar sensing studies exciting at 350 nm with an energy of 50 μJ/pulse, different solutions of BONDs with different metal ions, namely, Ag^{1+}, Co^{2+}, Cu^{2+}, Zn^{2+}, Fe^{3+}, Pt^{2+}, and Pt^{4+} (see Figures S6 and S7), none of which induces such important and systematic fluorescence intensity changes nor peak shift. This means that BONDs are selectively sensitive to Ni^{2+} ions, at least among the metal ions tested in our studies. Furthermore, focusing on the smallest concentration from which we observe spectroscopic changes, it is evident that the capability of BONDs to sense Ni^{2+} ions is extraordinary: in fact, we have observed PL variations already at a 1 pM Ni^{2+} concentration, which corresponds to less than 1 ppt. In addition, the sensor capability is excellent in a very wide detection range spacing from 1 to 10^4 pM and the detection time is just a few seconds. This paves the way for the functional use of BONDs in the ultrasensitive and straightforward detection of Ni^{2+} ions. For all these reasons, our nanosensors coupled with portable lasers or light-emitting devices and suitable detectors may be easily used as a real-time and in situ Ni^{2+} detector with very high accuracy and a promising selectivity.

For the sake of comparison, we recall that some of the most sensitive techniques currently employed in environmental pollutant sensing are high performance liquid chromatography (HPLC), mass spectrometry, and gas chromatography (GC). Mass spectrometry in particular can reach detection limits in the order of parts-per-trillion (ppt, ng/L) or even parts-per-quadrillion (ppq, pg/L).[52] However, these techniques are rather cumbersome and are not suitable for in situ measurements.[45] In the realm of nanotechnology, also sensors based on graphene,[53] carbon dots,[54−56] fluorescent quantum dots,[57] carbon nanotubes, and so on[45,58] have been often reported in the literature. Among these, very low detection thresholds have been obtained in particular for Hg ions: for example, Zhang et al. have reached attomolar mercury detection by combining graphene with Au NPs;[59] Amiri et al. have even achieved a zeptomolar detection limit by using double-stranded DNA on a gold electrode.[60] However, sometimes very low detection limits are then accompanied by rather long detection times, for example, in the range of 0.5−1 h, whereas in other cases they are paired with extremely narrow detection range (for example only from 1 to 10 nM).[45] BONDs are sensitive to low quantities as pg/L of Ni^{2+} ions in solution, and the sensitivity range is quite large (from 1pM to 100 nM at least). Thus, BONDs should help to overcome the above-mentioned problems. Interestingly, the spectroscopical modifications of the emission band shape are also reflected in the excited-state dynamics (Figure 5a). We compared time-resolved nanosecond decays of bare BONDs and BOND@Ni, as obtained by exposing the nanoparticle suspension to two different concentrations of ions (100 pM and 37 nM). Although the three kinetics are all in agreement with stretched-exponential-like trends, the corresponding lifetime derived by least-squares fitting increases from $\tau \sim 4.0$ ns for pristine BONDs, to $\tau = (4.3 \pm 0.2)$ ns for BOND@Ni 100 pM and finally to $\tau = (6.2 \pm 0.2)$ ns for BOND@Ni 37 nM. Instead, the stretching factor remains virtually identical ($\beta \approx 0.74$).

https://doi.org/10.1021/acsanm.3c00383
ACS Appl. Nano Mater. 2023, 6, 6036−6045

The intensity and lifetime can be related in some particular situations. In our case, the emission increases in the presence of Ni^{2+} reaching a value which is 4 times more than the initial value. At the same concentration, we measured the kinetics, obtaining a lifetime increase from 4.0 to 6.2 ns (1.5 factor). So, both intensity and lifetime increase their value, but the extent is quite different. This suggests that the relation between the two parameters is not simple and therefore that they can be used as two different and independent parameters which are controlled by the Ni^{2+} presence. Moreover, the emission redshift is in turn independent of both the intensity and the lifetime. Thus, the peak shift can be used as a third parameter to check the presence of Ni^{2+}. In summary, our B_2O_3 NPs are sensitive to Ni^{2+} ions by changes in three different observables: fluorescence intensity, peak shift, and excited-state lifetime. This allows to build a sensor potentially working by three different modes of detection, which drastically helps to reduce any interference with other photoluminescence species present in the same sample.

To investigate the enhancement mechanism, we performed ATR (Figure 5b) and FTIR (Figure S8) analyses, carried out on both BONDs and BOND@Ni 37 nM samples. The experiments highlight clear variations in the spectra. In particular, the peak centered at 3200 cm^{-1} undergoes a noticeable broadening, suggesting that the Ni^{2+} ions are attached to the OH groups decorating the BOND surface. At the same time, the intensity ratio between the peak at 1380−1450 and the peak at 1160−1220 cm^{-1} decreases, and a new broad band appears at 1080−1140 cm^{-1} after the addition of Ni^{2+} ions. Other minor variations are detectable also for the features peaked at smaller wavenumbers: a shoulder at about 600 cm^{-1} appears aside the peak at 630 cm^{-1}, while the peak at 810 cm^{-1} narrows down, and the intensity ratio between the two peaks at 630 and 810 cm^{-1} undergo measurable changes.

Beyond the great capability as a hypersensitive Ni^{2+} sensor, we verified the cytocompatibility of this new material in a proof-of-principle test. More in detail, BONDs have been tested on the human bronchial epithelial cell line 16-HBE, a well-established noninvasive model of lung cells[61,62] by evaluating the mitochondrial activity using the MTS assay. As reported in Figure 6, the sample displayed a typical dose−response trend of cell viability values and negligible cytotoxicity, also at very high concentrations (500 $\mu g\ mL^{-1}$) and for prolonged exposure (Figure 6b). Indeed, cell viability after 24 and 48 h of exposure is always higher than 70%, that is the normative limit of metabolic activity of the control. The high cytocompatibility observed is similar to that reported for other boron oxide nanoparticles (8−15 nm in diameter) explored as antimicrobial agents, where a cell viability of roughly 83% was obtained up to 5 mg mL^{-1}.[63] This result is promising, in view of the use of BONDs as nanosensors in a biomedical context.

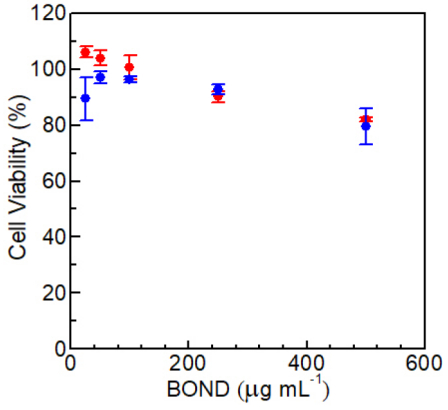

Figure 6. Cytocompatibility study of BONDs on 16-HBE after 24 (red) and 48 h (blue) of incubation.

4. CONCLUSION

We synthesized, for the first time, a novel type of Boron-based nanomaterial consisting of blue-emitting B_2O_3 nanodisks with a quasi-2D morphology. The synthesis is achieved by the sole employ of pulsed laser ablation of a Boron target in liquid, thus guaranteeing high purity of the endproduct in the absence of toxic side-products or reagents. Through the synergy of different experimental techniques, we characterized this new nanomaterial revealing B_2O_3 crystalline nature, a quasi-flat morphology, blue photoluminescence, and nontoxicity. The BONDs resulted to be highly sensitive to Ni^{2+} ions over a very wide detection range spacing from 1 pM to 40 nM. The interaction of BONDs with Ni^{2+} leads to independent modifications of emission intensity, peak position, and excited-state lifetime. This allows building a sensor potentially working down to the pg/L range, which could be used as a real-time and in situ Ni^{2+} detector with very high accuracy.

■ ASSOCIATED CONTENT

Supporting Information

The Supporting Information is available free of charge at https://pubs.acs.org/doi/10.1021/acsanm.3c00383.

Supplementary AFM, TEM, and XPS data; further structural characterization carried out via FTIR spectra acquisition; DSC/TGA studies; sensing tests involving different metal ions such as Ag^{1+}, Co^{2+}, Cu^{2+}, Zn^{2+}, Fe^{3+}, Pt^{2+}, and Pt^{4+} (PDF)

■ AUTHOR INFORMATION

Corresponding Author

Alice Sciortino − *Dipartimento di Fisica e Chimica Emilio Segrè, Università degli Studi di Palermo, Palermo 90128, Italy; ATeN Center, University of Palermo, Palermo 90128, Italy;* orcid.org/0000-0001-8361-3002; Email: alice.sciortino02@unipa.it

Authors

Angela Terracina − *Dipartimento di Fisica e Chimica Emilio Segrè, Università degli Studi di Palermo, Palermo 90128, Italy;* orcid.org/0000-0002-6906-4921

Nicolò Mauro − *Lab of Biocompatible Polymers, Department of Biological, Chemical and Pharmaceutical Sciences and Technologies (STEBICEF), University of Palermo, Palermo 90123, Italy;* orcid.org/0000-0003-0246-3474

Juliette Le Balle − *Dipartimento di Fisica e Chimica Emilio Segrè, Università degli Studi di Palermo, Palermo 90128, Italy*

Radian Popescu − *Laboratory for Electron Microscopy, Karlsruhe Institute of Technology, Karlsruhe 76131, Germany*

Michelangelo Scopelliti − *Dipartimento di Fisica e Chimica Emilio Segrè, Università degli Studi di Palermo, Palermo 90128, Italy; ATeN Center, University of Palermo, Palermo 90128, Italy;* orcid.org/0000-0001-5931-7668

https://doi.org/10.1021/acsanm.3c00383
ACS Appl. Nano Mater. 2023, 6, 6036−6045

Gianpiero Buscarino − *Dipartimento di Fisica e Chimica Emilio Segrè, Università degli Studi di Palermo, Palermo 90128, Italy; ATeN Center, University of Palermo, Palermo 90128, Italy;* orcid.org/0000-0001-8324-6783

Mara A. Utzeri − *Lab of Biocompatible Polymers, Department of Biological, Chemical and Pharmaceutical Sciences and Technologies (STEBICEF), University of Palermo, Palermo 90123, Italy*

Marco Cannas − *Dipartimento di Fisica e Chimica Emilio Segrè, Università degli Studi di Palermo, Palermo 90128, Italy*

Gennara Cavallaro − *Lab of Biocompatible Polymers, Department of Biological, Chemical and Pharmaceutical Sciences and Technologies (STEBICEF), University of Palermo, Palermo 90123, Italy; ATeN Center, University of Palermo, Palermo 90128, Italy;* orcid.org/0000-0003-0585-6564

Fabrizio Messina − *Dipartimento di Fisica e Chimica Emilio Segrè, Università degli Studi di Palermo, Palermo 90128, Italy; ATeN Center, University of Palermo, Palermo 90128, Italy;* orcid.org/0000-0002-2130-0120

Complete contact information is available at: https://pubs.acs.org/10.1021/acsanm.3c00383

Author Contributions

The manuscript was written through contributions of all authors. All authors have given approval to the final version of the manuscript.

Funding

This research was funded by the Italian MIUR PRIN 2017 "Candl2" Project Prot. no. 2017W75RAE and by Karlsruhe Nano Micro Facility (KNMF) − Proposal ID 2021-025-030071.

Notes

The authors declare no competing financial interest.

■ ACKNOWLEDGMENTS

We thank the LABAM group at the University of Palermo for support and stimulating discussions. AFM measurements were carried out at the laboratories of ATeN center − CHAB.

■ REFERENCES

(1) Tatiya, S.; Pandey, M.; Bhattacharya, S. Nanoparticles containing boron and its compounds—synthesis and applications: A review. *J. Micromanufacturing* **2020**, *3* (2), 159−173.

(2) Connell, T. L.; Risha, G. A.; Yetter, R. A.; Roberts, C. W.; Young, G. Boron and Polytetrafluoroethylene as a Fuel Composition for Hybrid Rocket Applications. *J. Propuls. Power* **2015**, *31* (1), 373−385.

(3) Jin, Y.; Xu, X.; Wang, X.; Dou, S.; Yang, Q.; Pan, L. Propulsive and combustion behavior of hydrocarbon fuels containing boron nanoparticles in a liquid rocket combustor. *Proc. Inst. Mech. Eng. Part G J. Aerosp. Eng.* **2022**, *236* (12), 2580−2591.

(4) Husain, E.; Narayanan, T. N.; Taha-Tijerina, J. J.; Vinod, S.; Vajtai, R.; Ajayan, P. M. Marine Corrosion Protective Coatings of Hexagonal Boron Nitride Thin Films on Stainless Steel. *ACS Appl. Mater. Interfaces* **2013**, *5* (10), 4129−4135.

(5) Cassabois, G.; Valvin, P.; Gil, B. Hexagonal boron nitride is an indirect bandgap semiconductor. *Nat. Photonics* **2016**, *10* (4), 262−266.

(6) Hao, J.; Tai, G.; Zhou, J.; Wang, R.; Hou, C.; Guo, W. Crystalline Semiconductor Boron Quantum Dots. *ACS Appl. Mater. Interfaces* **2020**, *12* (15), 17669−17675.

(7) Muzyka, K.; Sun, J.; Fereja, T. H.; Lan, Y.; Zhang, W.; Xu, G. Boron-doped diamond: current progress and challenges in view of electroanalytical applications. *Anal. Methods* **2019**, *11* (4), 397−414.

(8) Matkovich, V. I.; *Boron and Refractory Borides*; Springer: Berlin, 1977.

(9) Köster, R. Boron, Metallo-Boron Compounds and Boranes. Herausgeg. v.R. M. Adams. Interscience Publishers, a Division of John Wiley & Sons, New York-London-Sydney 1964. 1. Aufl., XXIII, 765 S., mehr. Abb. u. Tab., geb. £10.7.0. *Angew. Chem.* **1966**, *78* (4), 275−275.

(10) Mortensen, M. W.; Sørensen, P. G.; Björkdahl, O.; Jensen, M. R.; Gundersen, H. J. G.; Bjørnholm, T. Preparation and characterization of Boron carbide nanoparticles for use as a novel agent in T cell-guided boron neutron capture therapy. *Appl. Radiat. Isot.* **2006**, *64* (3), 315−324.

(11) Hawthorne, M. F. The Role of Chemistry in the Development of Boron Neutron Capture Therapy of Cancer. *Angew. Chem., Int. Ed. Engl.* **1993**, *32* (7), 950−984.

(12) Chan, W.-J.; Cho, H.-L.; Goudar, V.; Bupphathong, S.; Shu, C.-H.; Kung, C.; Tseng, F.-G. Boron-enriched polyvinyl-alcohol/boric-acid nanoparticles for boron neutron capture therapy. *Nanomedicine* **2021**, *16* (6), 441−452.

(13) Xu, T. T.; Zheng, J.-G.; Wu; Nicholls, A. W.; Roth, J. R.; Dikin, D. A.; Ruoff, R. S. Crystalline Boron Nanoribbons: Synthesis and Characterization. *Nano Lett.* **2004**, *4* (5), 963−968.

(14) Yamaguchi, M.; Pakdel, A.; Zhi, C.; Bando, Y.; Tang, D.-M.; Faerstein, K.; Shtansky, D.; Golberg, D. Utilization of multiwalled boron nitride nanotubes for the reinforcement of lightweight aluminum ribbons. *Nanoscale Res. Lett.* **2013**, *8* (1), 3.

(15) Ciuparu, D.; Klie, R. F.; Zhu, Y.; Pfefferle, L. Synthesis of Pure Boron Single-Wall Nanotubes. *J. Phys. Chem. B* **2004**, *108* (13), 3967−3969.

(16) Otten, C. J.; Lourie, O. R.; Yu, M.-F.; Cowley, J. M.; Dyer, M. J.; Ruoff, R. S.; Buhro, W. E. Crystalline Boron Nanowires. *J. Am. Chem. Soc.* **2002**, *124* (17), 4564−4565.

(17) Cao, L. M.; Zhang, Z.; Sun, L. L.; Gao, C. X.; He, M.; Wang, Y. Q.; Li, Y. C.; Zhang, X. Y.; Li, G.; Zhang, J.; Wang, W. K. Well-Aligned Boron Nanowire Arrays. *Adv. Mater.* **2001**, *13* (22), 1701−1704.

(18) Nagarajan, S.; Belaid, H.; Pochat-Bohatier, C.; Teyssier, C.; Iatsunskyi, I.; Coy, E.; Balme, S.; Cornu, D.; Miele, P.; Kalkura, N. S.; Cavaillès, V.; Bechelany, M. Design of Boron Nitride/Gelatin Electrospun Nanofibers for Bone Tissue Engineering. *ACS Appl. Mater. Interfaces* **2017**, *9* (39), 33695−33706.

(19) Chen, Q.; Li, W.-L.; Zhao, Y.-F.; Zhang, S.-Y.; Hu, H.-S.; Bai, H.; Li, H.-R.; Tian, W.-J.; Lu, H.-G.; Zhai, H.-J.; Li, S.-D.; Li, J.; Wang, L.-S. Experimental and Theoretical Evidence of an Axially Chiral Borospherene. *ACS Nano* **2015**, *9* (1), 754−760.

(20) Chen, Q.; Zhang, S.-Y.; Bai, H.; Tian, W.-J.; Gao, T.; Li, H.-R.; Miao, C.-Q.; Mu, Y.-W.; Lu, H.-G.; Zhai, H.-J.; Li, S.-D. Cage-Like B 41 + and B 42 2+ : New Chiral Members of the Borospherene Family. *Angew. Chemie Int. Ed.* **2015**, *54* (28), 8160−8164.

(21) Mannix, A. J.; Zhang, Z.; Guisinger, N. P.; Yakobson, B. I.; Hersam, M. C. Borophene as a prototype for synthetic 2D materials development. *Nat. Nanotechnol.* **2018**, *13* (6), 444−450.

(22) Chen, C.; Lv, H.; Zhang, P.; Zhuo, Z.; Wang, Y.; Ma, C.; Li, W.; Wang, X.; Feng, B.; Cheng, P.; Wu, X.; Wu, K.; Chen, L. Synthesis of bilayer borophene. *Nat. Chem.* **2022**, *14* (1), 25−31.

(23) Belyaev, I. B.; Zelepukin, I. V.; Pastukhov, A. I.; Shakhov, P. V.; Tikhonowski, G. V.; Popov, A. A.; Zakharkiv, A. Y.; Klimentov, S. M.; Garmash, A. A.; Zavestovskaya, I. N.; Deyev, S. M.; Kabashin, A. V. Study of IR Photoheating of Aqueous Solutions of Boron Nanoparticles Synthesized by Pulsed Laser Ablation for Cancer Therapy. *Bull. Lebedev Phys. Inst.* **2022**, *49* (6), 185−189.

(24) Pickering, A. L.; Mitterbauer, C.; Browning, N. D.; Kauzlarich, S. M.; Power, P. P. Room temperature synthesis of surface-functionalised boron nanoparticles. *Chem. Commun.* **2007**, *2* (6), 580−582.

(25) Johnston, H. L.; Hersh, H. N.; Kerr, E. C. Low Temperature Heat Capacities of Inorganic Solids. V. The Heat Capacity of Pure Elementary Boron in Both Amorphous and Crystalline Conditions between 13 and 305 K. Some Free Energies of Formation. *J. Am. Chem. Soc.* **1951**, *73* (3), 1112−1117.
(26) Wang, J.; Ma, F.; Liang, W.; Sun, M. Electrical properties and applications of graphene, hexagonal boron nitride (h-BN), and graphene/h-BN heterostructures. *Mater. Today Phys.* **2017**, *2*, 6−34.
(27) Tian, Y.; Guo, Z.; Zhang, T.; Lin, H.; Li, Z.; Chen, J.; Deng, S.; Liu, F. Inorganic Boron-Based Nanostructures: Synthesis, Optoelectronic Properties, and Prospective Applications. *Nanomaterials* **2019**, *9* (4), 538.
(28) Dzero, M.; Xia, J.; Galitski, V.; Coleman, P. Topological Kondo Insulators. *Annu. Rev. Condens. Matter Phys.* **2016**, *7* (1), 249−280.
(29) Tsierkezos, N. G.; Ritter, U.; Thaha, Y. N.; Downing, C. Application of multi-walled carbon nanotubes modified with boron oxide nanoparticles in electrochemistry. *Ionics (Kiel).* **2015**, *21* (11), 3087−3095.
(30) Kangallı, E.; Bayraktar, E. Preparation and characterization of poly(lactic acid)/boron oxide nanocomposites: Thermal, mechanical, crystallization, and flammability properties. *J. Appl. Polym. Sci.* **2022**, *139* (28), No. e52521.
(31) Ramachandran, R.; Jung, D.; Bernier, N. A.; Logan, J. K.; Waddington, M. A.; Spokoyny, A. M. Sonochemical Synthesis of Small Boron Oxide Nanoparticles. *Inorg. Chem.* **2018**, *57* (14), 8037−8041.
(32) Si, P. Z.; Zhang, M.; You, C. Y.; Geng, D. Y.; Du, J. H.; Zhao, X. G.; Ma, X. L.; Zhang, Z. D. Amorphous boron nanoparticles and BN encapsulating boron nano-peanuts prepared by arc-decomposing diborane and nitriding. *J. Mater. Sci.* **2003**, *38* (4), 689−692.
(33) Marzik, J. V.; Suplinskas, R. J.; Wilke, R. H. T.; Canfield, P. C.; Finnemore, D. K.; Rindfleisch, M.; Margolies, J.; Hannahs, S. T. Plasma synthesized doped B powders for MgB2 superconductors. *Phys. C Supercond. its Appl.* **2005**, *423* (3−4), 83−88.
(34) Bellott, B. J.; Noh, W.; Nuzzo, R. G.; Girolami, G. S. Nanoenergetic materials: boron nanoparticles from the pyrolysis of decaborane and their functionalisation. *Chem. Commun.* **2009**, No. 22, 3214.
(35) Shin, W. G.; Calder, S.; Ugurlu, O.; Girshick, S. L. Production and characterization of boron nanoparticles synthesized with a thermal plasma system. *J. Nanoparticle Res.* **2011**, *13* (12), 7187−7191.
(36) Pastukhov, A. I.; Belyaev, I. B.; Bulmahn, J. C.; Zelepukin, I. V.; Popov, A. A.; Zavestovskaya, I. N.; Klimentov, S. M.; Deyev, S. M.; Prasad, P. N.; Kabashin, A. V. Laser-ablative aqueous synthesis and characterization of elemental boron nanoparticles for biomedical applications. *Sci. Rep.* **2022**, *12* (1), 1−11.
(37) Fu, Z.; Williams, G. R.; Niu, S.; Wu, J.; Gao, F.; Zhang, X.; Yang, Y.; Li, Y.; Zhu, L.-M. Functionalized boron nanosheets as an intelligent nanoplatform for synergistic low-temperature photothermal therapy and chemotherapy. *Nanoscale* **2020**, *12* (27), 14739−14750.
(38) Amendola, V.; Meneghetti, M. What controls the composition and the structure of nanomaterials generated by laser ablation in liquid solution? *Phys. Chem. Chem. Phys.* **2013**, *15* (9), 3027−3046.
(39) Al-Kattan, A.; Ryabchikov, Y. V.; Baati, T.; Chirvony, V.; Sánchez-Royo, J. F.; Sentis, M.; Braguer, D.; Timoshenko, V. Y.; Estève, M.-A.; Kabashin, A. V. Ultrapure laser-synthesized Si nanoparticles with variable oxidation states for biomedical applications. *J. Mater. Chem. B* **2016**, *4* (48), 7852−7858.
(40) Sylvestre, J. P.; Poulin, S.; Kabashin, A. V.; Sacher, E.; Meunier, M.; Luong, J. H. T. Surface chemistry of gold nanoparticles produced by laser ablation in aqueous media. *J. Phys. Chem. B* **2004**, *108* (43), 16864−16869.
(41) Kabashin, A. V.; Meunier, M. Synthesis of colloidal nanoparticles during femtosecond laser ablation of gold in water. *J. Appl. Phys.* **2003**, *94* (12), 7941.
(42) EFSA Panel on Contaminants in the Food Chain (CONTAM). Scientific Opinion on the risks to animal and public health and the environment related to the presence of nickel in feed. *EFSA J.* **2015**, *13* (4), 4074.
(43) EFSA Panel on Contaminants in the Food Chain (CONTAM). Scientific Opinion on the risks to public health related to the presence of nickel in food and drinking water. *EFSA J.* **2015**, *13* (2), 4002.
(44) Ali, H.; Khan, E. Trophic transfer, bioaccumulation, and biomagnification of non-essential hazardous heavy metals and metalloids in food chains/webs—Concepts and implications for wildlife and human health. *Hum. Ecol. Risk Assess. An Int. J.* **2019**, *25* (6), 1353−1376.
(45) Zhang, Y.; Zhu, Y.; Zeng, Z.; Zeng, G.; Xiao, R.; Wang, Y.; Hu, Y.; Tang, L.; Feng, C. Sensors for the environmental pollutant detection: Are we already there? *Coord. Chem. Rev.* **2021**, *431*, 213681.
(46) Stadelmann, P. *jems*; http://www.jems-swiss.ch/ (accessed 2022-04-01).
(47) Burianek, M.; Birkenstock, J.; Mair, P.; Kahlenberg, V.; Medenbach, O.; Shannon, R. D.; Fischer, R. X. High-pressure synthesis, long-term stability of single crystals of diboron trioxide, B_2O_3, and an empirical electronic polarizability of [3]B3+. *Phys. Chem. Miner.* **2016**, *43* (7), 527−534.
(48) Zhang, C. C.; Gao, X.; Yilmaz, B. Development of FTIR Spectroscopy Methodology for Characterization of Boron Species in FCC Catalysts. *Catalysts* **2020**, *10* (11), 1327.
(49) Sciortino, A.; Marino, E.; Dam, B. v.; Schall, P.; Cannas, M.; Messina, F. Solvatochromism Unravels the Emission Mechanism of Carbon Nanodots. *J. Phys. Chem. Lett.* **2016**, *7* (17), 3419−3423.
(50) Yuan, J.; Wang, E.; Chen, Y.; Yang, W.; Yao, J.; Cao, Y. Doping mode, band structure and photocatalytic mechanism of B-N-codoped TiO_2. *Appl. Surf. Sci.* **2011**, *257* (16), 7335−7342.
(51) Li, D.; Ching, W. Y. Electronic structures and optical properties of low- and high-pressure phases of crystalline B_2O_3. *Phys. Rev. B* **1996**, *54* (19), 13616−13622.
(52) Mooney, D.; Coxon, C.; Richards, K. G.; Gill, L. W.; Mellander, P.-E.; Danaher, M. A new sensitive method for the simultaneous chromatographic separation and tandem mass spectrometry detection of anticoccidials, including highly polar compounds, in environmental waters. *J. Chromatogr. A* **2020**, *1618*, 460857.
(53) Chen, D.; Feng, H.; Li, J. Graphene Oxide: Preparation, Functionalization, and Electrochemical Applications. *Chem. Rev.* **2012**, *112* (11), 6027−6053.
(54) Bruno, F.; Sciortino, A.; Buscarino, G.; Cannas, M.; Gelardi, F. M.; Messina, F.; Agnello, S. Sensing of Transition Metals by Top-Down Carbon Dots. *Appl. Sci.* **2021**, *11* (21), 10360.
(55) Bruno, F.; Sciortino, A.; Buscarino, G.; Soriano, M. L.; Ríos, Á.; Cannas, M.; Gelardi, F.; Messina, F.; Agnello, S. A comparative study of top-down and bottom-up carbon nanodots and their interaction with mercury ions. *Nanomaterials* **2021**, *11* (5), 1265.
(56) Bruno, F.; Sciortino, A.; Buscarino, G.; Cannas, M.; Gelardi, F. M.; Agnello, S.; Messina, F. Fluorescent Carbon Nanodots as Sensors of Toxic Metal Ions and Pesticides. *Eng. Proc.* **2021**, *6*, 21.
(57) Huang, D.; Niu, C.; Wang, X.; Lv, X.; Zeng, G. Turn-On" Fluorescent Sensor for Hg 2+ Based on Single-Stranded DNA Functionalized Mn:CdS/ZnS Quantum Dots and Gold Nanoparticles by Time-Gated Mode. *Anal. Chem.* **2013**, *85* (2), 1164−1170.
(58) Yin, H.; Zhou, Y.; Xu, J.; Ai, S.; Cui, L.; Zhu, L. Amperometric biosensor based on tyrosinase immobilized onto multiwalled carbon nanotubes-cobalt phthalocyanine-silk fibroin film and its application to determine bisphenol A. *Anal. Chim. Acta* **2010**, *659* (1−2), 144−150.
(59) Zhang, Y.; Zeng, G. M.; Tang, L.; Chen, J.; Zhu, Y.; He, X. X.; He, Y. Electrochemical Sensor Based on Electrodeposited Graphene-Au Modified Electrode and NanoAu Carrier Amplified Signal Strategy for Attomolar Mercury Detection. *Anal. Chem.* **2015**, *87* (2), 989−996.
(60) Amiri, S.; Navaee, A.; Salimi, A.; Ahmadi, R. Zeptomolar detection of Hg 2+ based on label-free electrochemical aptasensor: One step closer to the dream of single atom detection. *Electrochem. commun.* **2017**, *78*, 21−25.

https://doi.org/10.1021/acsanm.3c00383
ACS Appl. Nano Mater. 2023, 6, 6036−6045

(61) Mauro, N.; Schillaci, D.; Varvarà, P.; Cusimano, M. G.; Geraci, D. M.; Giuffrè, M.; Cavallaro, G.; Maida, C. M.; Giammona, G. Branched High Molecular Weight Glycopolypeptide With Broad-Spectrum Antimicrobial Activity for the Treatment of Biofilm Related Infections. *ACS Appl. Mater. Interfaces* **2018**, *10* (1), 318−331.
(62) Porsio, B.; Craparo, E. F.; Mauro, N.; Giammona, G.; Cavallaro, G. Mucus and Cell-Penetrating Nanoparticles Embedded in Nano - into - Micro Formulations for Pulmonary Delivery of Ivacaftor in Patients with Cystic Fibrosis. *ACS Appl. Mater. Interfaces* **2018**, *10* (1), 165−181.
(63) Elabbasy, M. T.; Algahtani, F. D.; Al-Harthi, H. F.; Abd El-Kader, M. F. H.; Eldrehmy, E. H.; Abd El-Rahman, G. I.; El-Morsy, M. A.; Menazea, A. A. Optimization of compositional manipulation for hydroxyapatite modified with boron oxide and graphene oxide for medical applications. *J. Mater. Res. Technol.* **2022**, *18*, 5419−5431.

Recommended by ACS

Chemical Influence of Carbon Interface Layers in Metal/Oxide Resistive Switches
Deok-Yong Cho, Ilia Valov, *et al.*
MARCH 29, 2023
ACS APPLIED MATERIALS & INTERFACES
READ

Density-Induced Joule-Heating Characteristics of Nanocarbon Aerogels: Implications for Tunable Electrothermal Behaviors
Dong Xia, Peng Huang, *et al.*
APRIL 20, 2023
ACS APPLIED NANO MATERIALS
READ

Bismuth Oxychloride Nanoflakes Enabled High Sensitivity Colorimetric UV Dosimetry
Kyle Troche, Fernando H. Garzon, *et al.*
APRIL 03, 2023
ACS APPLIED NANO MATERIALS
READ

Sustainable Approach of Using *Arundo donax* Leaves Reinforced Cement Mortar/Fly Bottom Ash Composites
Houda Hachem, Daoued Mihoubi, *et al.*
MARCH 21, 2023
ACS OMEGA
READ

Get More Suggestions >

https://doi.org/10.1021/acsanm.3c00383
ACS Appl. Nano Mater. 2023, 6, 6036−6045